Contactless Microwave Tomography via MIMO GPR

Ilaria Catapano, *Member, IEEE*, Gianluca Gennarelli, Giuseppe Esposito, Giovanni Ludeno, Yan Su, Zongyu Zhang, and Francesco Soldovieri

***Abstract*— This letter presents an imaging approach for multiple input–multiple output ground penetrating radar (MIMO GPR) systems working in down-looking contactless mode. The approach exploits a linear approximation of the scattering phenomenon and is based on a ray-based propagation model, which takes into account the presence of the air–soil interface. Accordingly, the interface reflection point (IRP) concept is extended to the case of MIMO GPR. The proposed approach performs the imaging in the 2-D scalar case and applies the truncated singular value decomposition regularization scheme to perform the inversion. The effectiveness of the approach is assessed by processing synthetic and real data. The real data are referred to the lunar soil and have been collected by means of the Lunar Regolith Penetrating Radar (LRPR), installed on the Chang'E-5 (CE-5) lander.**

***Index Terms*— Inverse scattering, microwave tomography, multiple input–multiple output (MIMO) radar, radar imaging.**

I. Introduction

THE ongoing advances in multiple input–multiple output ground penetrating radar (MIMO GPR) technology affect subsurface imaging positively. Indeed, a MIMO GPR gathers a larger amount of useful data compared to a bistatic system and the increased amount of collected information yields an improvement in terms of target detection and reconstruction accuracy. Of course, specific data processing strategies are required [1]; accordingly, several approaches have been proposed to process data collected by down-looking and forward-looking MIMO GPR, and their performance has been assessed by performing numerical simulations or experimental tests, mainly in controlled conditions [2], [3], [4], [5], [6], [7], [8], [9], [10].

In this framework, this letter proposes an imaging strategy for data collected by a down-looking MIMO GPR operating at a non-negligible distance, in terms of the probing wavelength, from the air–soil interface.

The imaging approach is formulated as a 2-D scalar inverse scattering problem, where the imaging plane is defined by the straight line along which the antennas are located and the direction normal to the air–soil interface (depth). The scattering phenomenon is described by a ray-based model [11] and the presence of the air–soil interface is accounted for by exploiting the interface reflection point (IRP) concept, already presented for a multi-monostatic configuration [11], [12]. In this study, as a novel aspect, the IRP-based inversion approach is extended to the case of MIMO GPR.

The main advantage of the proposed imaging approach is the flexibility, which allows its use in the case of an equal number of transmitting and receiving antennas as well as in the case of M transmitting antennas and N receiving ones, with $M \neq N$. On the other hand, being based on the 2-D scalar scattering model, the approach requires that antennas must be located in the imaging plane.

The reconstruction capabilities of the approach are assessed by processing synthetic and real data. A virtual experiment was carried out by using GPRMax [13] to generate scattered field data and provides a proof of concept of the achievable performance. Real data are referred to the lunar subsoil and were collected by the Lunar Regolith Penetrating Radar (LRPR), installed at the bottom of the Chang'E-5 (CE-5) lander [14]. These data have been already processed and interpreted in [14] and the consistency between previously published results [14], [15] and those herein provided gives proof of the imaging capabilities of the approach against experimental data.

The letter is organized as follows. Section II describes the imaging approach. Section III shows the reconstruction capabilities against synthetic data, while Section IV deals with the analysis of real data. Conclusions and future perspectives are given in Section V.

II. Contactless MIMO GPR Imaging

Let us consider the reference half-space scenario sketched in Fig. 1, where the upper half-space is air while the lower one is soil having a relative permittivity ε_s. The target has a relative permittivity ε_t and resides in the investigation domain D, which is probed by an array of M transmitting and N receiving antennas located along a line at a distance h above the air–soil interface. Specifically, when the pth antenna transmits, all the N-receiving antennas measure the backscattered field.

By assuming the linear scattering model in [12], [16], and [17] and omitting the time factor $\exp(j\omega t)$, the integral equation (1) defines the frequency domain relationship

Manuscript received 30 December 2022; revised 2 March 2023; accepted 6 March 2023. Date of publication 16 March 2023; date of current version 24 March 2023. *(Corresponding author: Francesco Soldovieri.)*

Ilaria Catapano, Gianluca Gennarelli, Giuseppe Esposito, Giovanni Ludeno, and Francesco Soldovieri are with the Institute for Electromagnetic Sensing of the Environment (IREA)—National Research Council of Italy (CNR), 80128 Naples, Italy (e-mail: soldovieri.f@irea.cnr.it).

Yan Su and Zongyu Zhang are with the National Astronomical Observatories, Chinese Academy of Sciences, Beijing 100107, China, and also with the School of Astronomy and Space Science, University of Chinese Academy of Sciences, Beijing 101408, China.

Digital Object Identifier 10.1109/LGRS.2023.3257540

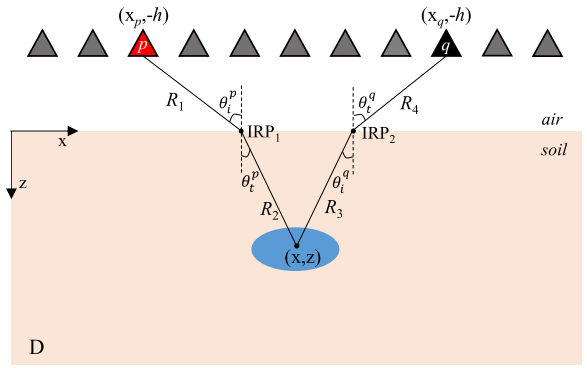

Fig. 1. Reference scenario.

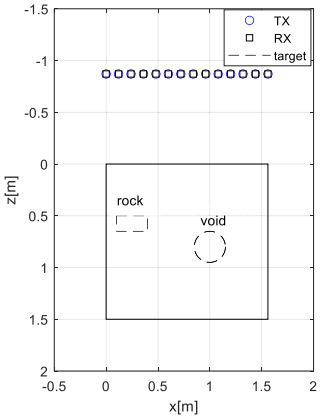

Fig. 2. Virtual experiment—reference scenario.

between the scattered field E_s and the unknown contrast $\chi(r) = (\varepsilon_t/\varepsilon_s) - 1$ relating the permittivity of the target to that of the hosting soil

$$E_s(\boldsymbol{r}_q, \boldsymbol{r}_p, \omega) = \frac{-j\omega\sqrt{\varepsilon_s}}{2\pi c} \iint_D \frac{T_{12}T_{21}}{\sqrt{(R_1+R_2)(R_3+R_4)}} \times \exp\left\{-\frac{j\omega}{c}\left((R_1+R_4)+\sqrt{\epsilon}_s(R_3+R_4)\right)\right\} \times \chi(r)dr = L[\chi]. \quad (1)$$

In (1), $E_s(\boldsymbol{r}_q, \boldsymbol{r}_p, \omega)$ is the scattered field at the angular frequency ω when the pth antenna at $\boldsymbol{r}_p = (x_p, -h)$ transmits the probing wave and the qth antenna at $\boldsymbol{r}_q = (x_q, -h)$ collects the backscattered signal. Moreover, $c \approx 3e{+}8$ m/s denotes the electromagnetic wave speed in air; T_{12} and T_{21} are the air–soil and soil–air Fresnel's transmission coefficients

$$T_{12} = \frac{2\cos\left(\theta_i^p\right)}{\cos\left(\theta_i^p\right) + \sqrt{\epsilon}_s\cos\left(\theta_t^p\right)}$$
$$T_{21} = \frac{2\sqrt{\varepsilon}_s\cos(\theta_i^q)}{\sqrt{\varepsilon}_s\cos\left(\theta_i^q\right) + \cos(\theta_t^q)}. \quad (2)$$

R_1–R_4 identify the length of the ray path (see Fig. 1)

$$R_1 = \frac{h}{\cos\left(\theta_i^p\right)}, \quad R_2 = \frac{z}{\cos\left(\theta_t^p\right)}$$
$$R_3 = \frac{z}{\cos\left(\theta_i^q\right)}, \text{ and } R_4 = \frac{h}{\cos\left(\theta_t^q\right)}. \quad (3)$$

$L{:}\mathcal{L}^2(\mathrm{D}) \rightarrow \mathcal{L}^2(\Gamma \times \Omega)$ is the linear operator mapping the unknown in D into the data space $\mathcal{L}^2(\Gamma \times \Omega)$, where Γ accounts for the MIMO measurement setup and $\Omega \in [\omega_{\min}, \omega_{\max}]$ is the working angular frequency range.

The transmission coefficients as well as the ray paths depend on the incidence angles (θ_i^p, θ_i^q) and the transmission ones (θ_t^p, θ_t^q). These angles depend on the position of IRP_1 and IRP_2, which are determined by solving two non-linear equations, for each transmitting/receiving antenna pair and each point $r(x, z)$ in D. Specifically, by resorting to the considerations made in [16] for the multi-monostatic configuration and according to the second Snell's law, the angles $(\theta_i^{p,q}, \theta_t^{p,q})$ are related to each other as

$$\sin\left(\theta_i^p\right) = \sqrt{\varepsilon}_s\sin\left(\theta_t^p\right) \text{ and } \sqrt{\varepsilon}_s\sin\left(\theta_i^q\right) = \sin\left(\theta_t^q\right) \quad (4)$$

and the following two equations are solved with respect to the unknown angles (θ_i^p, θ_t^q), taking values in the range $[0, \pi/2]$:

$$|x - x_p| = h\tan\left(\theta_i^p\right) + \frac{z\sin\left(\theta_i^p\right)}{\sqrt{\epsilon_s - \sin^2\left(\theta_i^p\right)}} \quad (5)$$

$$|x - x_q| = h\tan\left(\theta_t^q\right) + \frac{z\sin\left(\theta_t^q\right)}{\sqrt{\epsilon_s - \sin^2\left(\theta_t^q\right)}}. \quad (6)$$

Once all the quantities defining the kernel of (1) have been determined, (1) is discretized by using the method of moments and the discretized inverse problem is solved by means of the truncated singular value decomposition (TSVD) regularization method [12], [17]. Therefore, the reconstructed contrast vector is given by

$$\tilde{\boldsymbol{\chi}} = \sum_{n=1}^{N_t} \frac{\langle \boldsymbol{E}_s \boldsymbol{u}_n \rangle}{\sigma_n} \boldsymbol{v}_n \quad (7)$$

where $\langle , \rangle$ is the inner product in the data space, σ_n is the nth singular value of the matrix $\mathbf{L}$ discretizing the operator L, and $\boldsymbol{u}_n$ and $\boldsymbol{v}_n$ are its right and left singular vectors, respectively. The regularization parameter N_t is the number of the considered singular values and it is fixed as a trade-off between the resolution and stability of the solution. The modulus of the regularized contrast vector $\boldsymbol{\chi}$ in (7) defines a spatial map referred to as a tomographic image of the domain D.

III. Numerical Assessment

This section provides a proof of concept of the effectiveness of the imaging approach against virtual data, generated by using GPRMax and referred to the scenario sketched in Fig. 2.

The MIMO array is 1.56 m long and composed of $M = N = 14$ Tx/Rx antennas, which are 12 cm evenly spaced and located at a height of 0.87 m above the air–soil interface. The antennas operate at the center frequency of 2 GHz and probe a regolith soil medium ($\varepsilon_s = 2.5$ and $\sigma_s = 1e-4$ S/m) wherein a granite ($\varepsilon_t = 5.45$ and $\sigma_t = 2.3e-8$ S/m) rock of size 30 × 10 cm and a circular cavity of radius 15 cm are buried. The raw data have been simulated by using as a probing signal a Ricker pulse with a central frequency of 2 GHz. For each transmitting

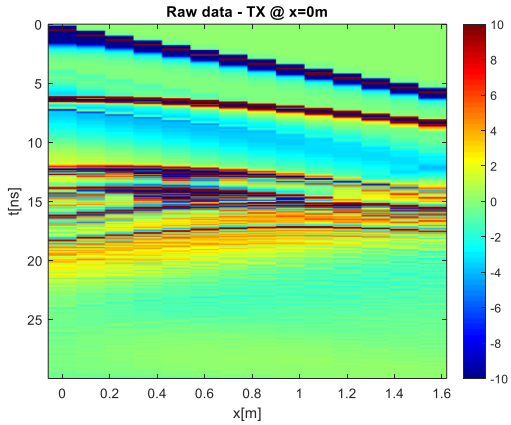

Fig. 3. Virtual experiment—radargram referred to the transmitting antenna at $x = 0$ m and $z = -0.87$ m.

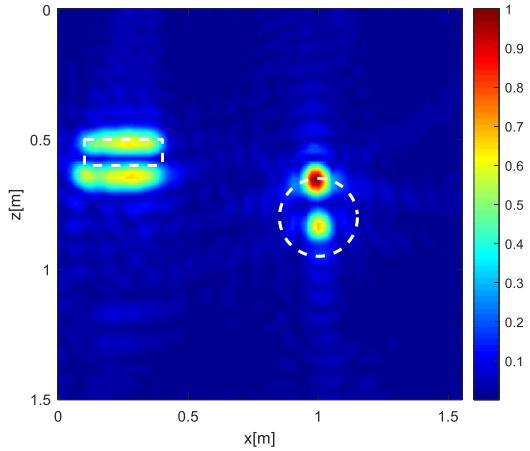

Fig. 4. Virtual experiment—tomographic image as normalized to its maximum amplitude.

antenna, the radar signal is collected at $N = 14$ measurement points. The raw radargram referred to the transmitting antenna at $x = 0$ m and $z = -0.87$ m is illustrated in Fig. 3.

All collected radargrams have been processed in time domain (TD) by setting the time zero at 0.51 ns and applying a time gating [18] at $t_g = 10$ ns in order to filter the direct antenna coupling and reflection from the air–soil interface. Then, TD data have been transformed into the frequency domain. By observing the data spectrum, the useful frequency range has been set from 1500 up to 2500 MHz. This frequency interval has been sampled with a 50 MHz step. The TSVD regularization parameter Nt has been set in order to filter out all the singular values whose amplitude is 20 dB lower than the maximum one.

Fig. 4 displays the tomographic image as normalized to its maximum value and the dashed white line represents the simulated targets. Fig. 4 assesses the imaging capabilities of the proposed approach since an accurate localization of both targets is achieved. Specifically, the position of the upper edge of the targets is exactly localized, while the lower ones are shifted upward (cavity) or downward (rock) as expected being the signal propagation velocity into the targets different from that assumed in the inversion model (electromagnetic velocity in the soil) [19].

IV. Experimental Assessment

This section deals with the results referred to the data gathered by the LRPR installed at the bottom of the CE-5 lander. CE-5 probe was launched successfully on 24 November 2020 and landed at the north Oceanus Procellarum. It returned 1731 g of both lunar surface and subsurface regolith by scooping and drilling. CE-5 lander carried an LRPR, which is the first ultra wide band (UWB) MIMO GPR deployed for planetary exploration. CE-5 successfully guided the sample drilling process and revealed the interior structure of the local regolith of ejecta deposit in the degraded Xu Guangqi crater with a diameter of ~463 m and a distance of ~400 m. The LRPR conducted seven GPR measurements, including three background measurements, one pre-drilling observation, and three post-drilling observations. The background measurements were taken in free space, 200 km above the lunar surface, and are not taken into account in this study. Pre- and post-drilling data here considered have been already processed and interpreted by using a migration approach [14], [15].

The LPRR operates in the 1–3 GHz band and exploits an array of 12 Vivaldi antennas covering the CE-5 drilling area. Antennas numbered from 1 to 10 are located in a line alongside the drilling pipe at height $h = 0.877$ m from the air–soil interface. The distance between two nearby antennas is 12 cm, except between antenna 7 and antenna 8, whose distance is 60 cm. The other two antennas (i.e., antennas 11 and 12) are mounted separately. The reader can refer to [14] for a detailed description of LRPR and its working parameters.

The LRPR pre-drilling (Pre) dataset and the three post-drilling ones (Post1–Post3) are herein considered. Specifically, MIMO data referred to the antennas numbered from 1 to 10 are processed, whereas those referred to antennas 11 and 12 are neglected, being these antennas outside the vertical plane wherein the imaging problem is formulated.

The proposed imaging strategy exploits the scattered field data in the frequency domain; therefore, TD data are transformed by means of the fast Fourier transform (FFT) algorithm by taking into account the effective frequency range of the data, which is selected by observing the behavior of data spectrum on a logarithmic scale.

Herein, the considered TD data are the result of a pre-processing stage, which includes sample time calibration, bandpass filtering, cable delay correction, and background removal; the pre-processing steps have been described in detail in [14]. Furthermore, the time gating procedure is applied in order to reduce the signal contribution due to the air–soil interface.

Fig. 5 shows the normalized average data spectrum of the four considered datasets and it turns out that the effective frequency band of the pre-processed data goes from $f_{\min} = 730$ MHz to $f_{\max} = 2.35$ GHz. Note that 73 evenly spaced frequencies have been considered in this range. Before transforming the data in the frequency domain, the energy loss occurring due to the geometric spreading associated with the propagation into the soil has been compensated by applying a gain function. This operation is done by multiplying the

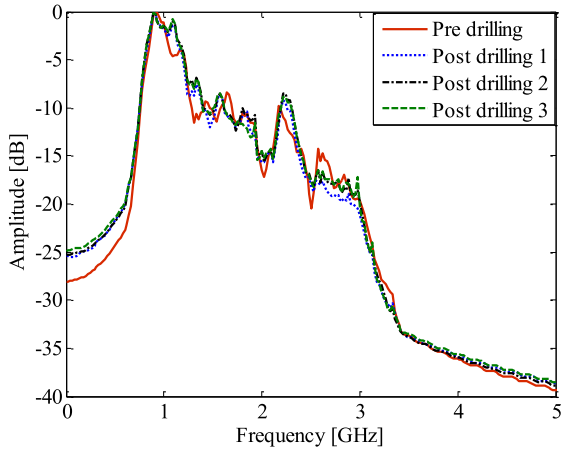

Fig. 5. Average data spectrum: red solid line—pre-drilling data; blue dotted line—post-drilling 1 data; black dashed-dotted line—post-drilling 2 data; and green dashed line—post-drilling 3 data.

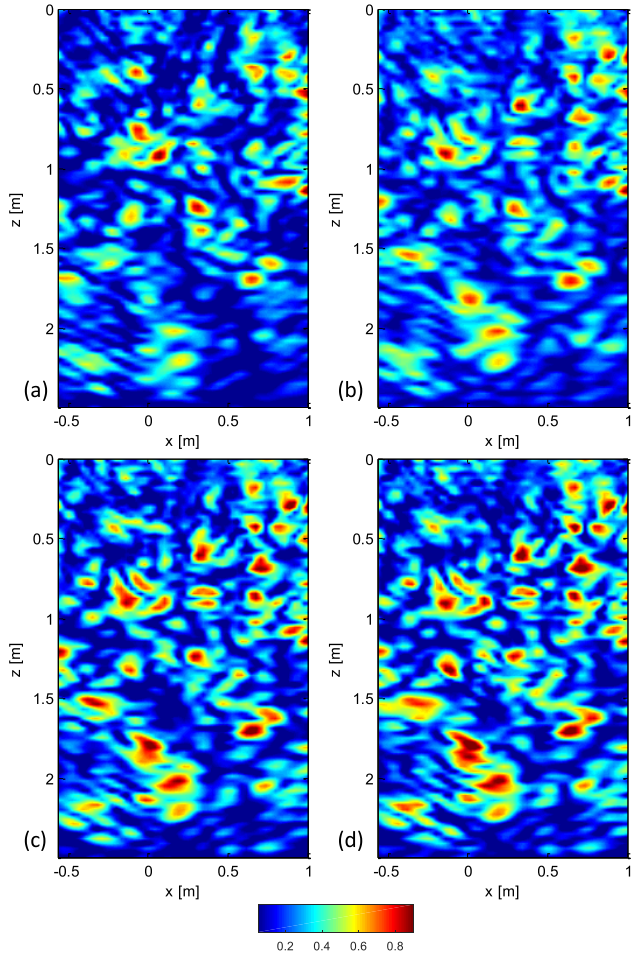

Fig. 6. Real experiment—tomographic images each one as normalized to its maximum amplitude, datasets (a) pre, (b) post 1, (c) post 2, and (d) post 3.

pre-processed data by the following function:

$$g(t) = \alpha \left(\frac{t}{2} \frac{c}{\sqrt{\varepsilon_s}} \right)^2 \tag{8}$$

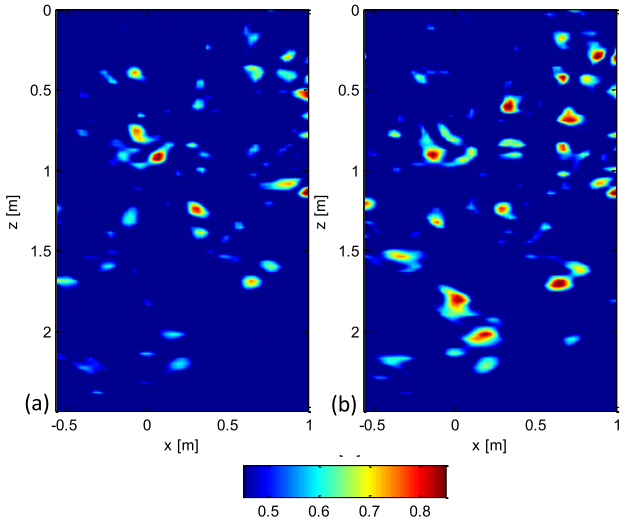

Fig. 7. Real experiment—tomographic images. (a) Pre-drilling and (b) post–drilling (multiplication of images).

where α is a scaling coefficient expressed in m^{-2} so that $g(t)$ is an a-dimensional function. In (8) t is the travel time and ε_s is the average relative permittivity of the lunar soil, whose value is set at 2.48 according to the analysis in [14]. It should be stressed that the quadratic function defined by (8) may attenuate very shallow targets. However, such a function was chosen to attenuate the residual clutter due to the reflection from the air–soil interface, which was not entirely removed by the previous preprocessing steps.

Fig. 6(a)–(d) shows the tomographic images referred to the four considered datasets achieved by considering the parameter N_t in the TSVD inversion (7) in such a way as to filter out all the singular values whose amplitude is 15 dB lower than the maximum one. Note that each image is normalized with respect to its maximum value.

Fig. 7 shows the comparison of the tomographic images before [see Fig. 7(a)] and after [see Fig. 7(b)] drilling. Note that Fig. 7(a) is the same as that of Fig. 6(a) but its color scale has been changed in order to emphasize the stronger scatterers. Conversely, Fig. 7(b) has been achieved by multiplying the results (images) in Fig. 6(b)–(d) and computing the cubic root. This is a simple way of combining tomographic images referred to the same scenario, i.e., the probed lunar soil after the drilling and accounting for the common reconstructed anomalies.

The pre- and post-drilling images in Fig. 6 and their corresponding combination in Fig. 7 reveal that the position of some scatterers in the subsoil is varied probably because a single or a cluster of dense fragments might have been crushed. This result is coherent with those reported in [14] and [15].

V. Conclusion and Future Perspectives

MIMO radar technology improves the effectiveness of GPR surveys in terms of target reconstruction accuracy but also requires specific approaches capable of accounting for the new kind and increased amount of data. In this frame, a microwave tomographic approach designed to process MIMO data collected by means of an arbitrary contactless GPR system made

up of M transmitting antennas and N receiving ones has been proposed. The approach faces the imaging as an inverse scattering problem and exploits a ray-based model of the scattering phenomenon. Specifically, the approach extends the IRP concept previously introduced for monostatic GPR to MIMO GPR.

Results referred to both simulated and experimental data corroborate the reconstruction capabilities in terms of accurate localization of the targets.

The analysis of the spatial resolution limits, how they depend on the number of transmitting and receiving antennas, and the improvements with respect to a multi-monostatic measurement configuration are under investigation and will be the subject of future work. The extension of the MIMO approach to the 3-D case will be also considered by generalizing the results recently published in [20].

ACKNOWLEDGMENT

The authors would like to thank the Ground Research and Application System Team Members from National Astronomical Observatories, Beijing, China, for their contribution to data receiving and release. Chang'E-5 (CE-5) radar data can access from the link http://www.dx.doi.org/10.12350/CLPDS.GRAS.CE5.LRPR-01.vA.

REFERENCES

[1] R. Persico, "On the role of measurement configuration in contactless GPR data processing by means of linear inverse scattering," *IEEE Trans. Antennas Propag.*, vol. 54, no. 7, pp. 2062–2071, Jul. 2006.

[2] X. Zhuge, A. G. Yarovoy, T. Savelyev, and L. Ligthart, "Modified Kirchhoff migration for UWB MIMO array-based radar imaging," *IEEE Trans. Geosci. Remote Sens.*, vol. 48, no. 6, pp. 2692–2703, Jun. 2010.

[3] T. Jin, J. Lou, and Z. Zhou, "Extraction of landmine features using a forward-looking ground-penetrating radar with MIMO array," *IEEE Trans. Geosci. Remote Sens.*, vol. 50, no. 10, pp. 4135–4144, Oct. 2012.

[4] J. Yang, T. Jin, X. Huang, J. Thompson, and Z. Zhou, "Sparse MIMO array forward-looking GPR imaging based on compressed sensing in clutter environment," *IEEE Trans. Geosci. Remote Sens.*, vol. 52, no. 7, pp. 4480–4494, Jul. 2014.

[5] Z. Zeng, J. Li, L. Huang, X. Feng, and F. Liu, "Improving target detection accuracy based on multipolarization MIMO GPR," *IEEE Trans. Geosci. Remote Sens.*, vol. 53, no. 1, pp. 15–24, Jan. 2015.

[6] F. Soldovieri, G. Gennarelli, I. Catapano, D. Liao, and T. Dogaru, "Forward-looking radar imaging: A comparison of two data processing strategies," *IEEE J. Sel. Topics Appl. Earth Observ. Remote Sens.*, vol. 10, no. 2, pp. 562–571, Feb. 2017.

[7] H. Liu, Z. Long, B. Tian, F. Han, G. Fang, and Q. H. Liu, "Two-dimensional reverse-time migration applied to GPR with a 3-D-to-2-D data conversion," *IEEE J. Sel. Topics Appl. Earth Observ. Remote Sens.*, vol. 10, no. 10, pp. 4313–4320, Oct. 2017.

[8] W. Zhang and A. Hoorfar, "MIMO ground penetrating radar imaging through multilayered subsurface using total variation minimization," *IEEE Trans. Geosci. Remote Sens.*, vol. 57, no. 4, pp. 2107–2115, Apr. 2019.

[9] A. Srivastav, P. Nguyen, M. McConnell, K. A. Loparo, and S. Mandal, "A highly digital multiantenna ground-penetrating radar (GPR) system," *IEEE Trans. Instrum. Meas.*, vol. 69, no. 10, pp. 7422–7436, Oct. 2020.

[10] K. Tan and X. Chen, "Fast 3-D image reconstruction on nonregular UWB sparse MIMO planar array using scaling techniques," *IEEE Trans. Microw. Theory Techn.*, vol. 69, no. 1, pp. 222–234, Jan. 2021.

[11] I. Catapano, L. Crocco, Y. Krellmann, G. Triltzsch, and F. Soldovieri, "Tomographic airborne ground penetrating radar imaging: Achievable spatial resolution and on-field assessment," *ISPRS J. Photogramm. Remote Sens.*, vol. 92, pp. 69–78, Jun. 2014.

[12] I. Catapano, G. Gennarelli, G. Ludeno, C. Noviello, G. Esposito, and F. Soldovieri, "Contactless ground penetrating radar imaging: State of the art, challenges, and microwave tomography-based data processing," *IEEE Geosci. Remote Sens. Mag.*, vol. 10, no. 1, pp. 251–273, Mar. 2022.

[13] Accessed: Dec. 28, 2022. [Online]. Available: https://www.gprmax.com/last

[14] Y. Su et al., "Hyperfine structure of regolith unveiled by Chang'E-5 lunar regolith penetrating radar," *IEEE Trans. Geosci. Rem. Sens.*, vol. 60, 2022, Art. no. 5110414.

[15] J. Feng, M. A. Siegler, and M. N. White, "Shallow regolith structure and obstructions detected by lunar regolith penetrating radar at Chang'E-5 drilling site," *Remote Sens.*, vol. 14, no. 14, p. 3378, Jul. 2022.

[16] W. C. Chew, *Waves Fields Inhomogeneous Media*, 2nd ed. New York, NY, USA: Wiley, 1995.

[17] M. Bertero and P. Boccacci, *Introduction to Inverse Problems in Imaging*. Bristol, U.K.: Institute of Physics, 1998.

[18] D. J. Daniels, *Ground Penetrating Radar*. Hoboken, NJ, USA: Wiley, 2005.

[19] R. Persico, F. Soldovieri, and G. Leone, "A microwave tomographic imaging approach for multibistatic configuration: The choice of the frequency step," *IEEE Trans. Instrum. Meas.*, vol. 55, no. 6, pp. 1926–1934, Dec. 2006.

[20] G. Gennarelli, C. Noviello, G. Ludeno, G. Esposito, F. Soldovieri, and I. Catapano, "Three-dimensional ray-based tomographic approach for contactless GPR imaging," *IEEE Trans. Geosci. Remote Sens.*, vol. 61, 2023, Art. no. 2000614, doi: 10.1109/TGRS.2023.3250740.

Open Access funding provided by 'Consiglio Nazionale delle Ricerche-CARI-CARE' within the CRUI CARE Agreement